International Journal of Refractory Metals & Hard Materials 86 (2020) 105112

Contents lists available at ScienceDirect

International Journal of Refractory Metals & Hard Materials

journal homepage: www.elsevier.com/locate/IJRMHM

Microstructure and properties of laser cladded B_4C/TiC/Ni-based composite coating

Yu Zhao[a,b], Tianbiao Yu[a,b,*], Jiayu Sun[c], Shengxin Jiang[d]

[a] School of Mechanical Engineering and Automation, Northeastern University, Shenyang 110819, China
[b] Liaoning Provincial Key Laboratory of High-end Equipment Intelligent Design and Manufacturing Technology, Northeastern University, Shenyang 110819, China
[c] Deformation Processing Institute for Materials Research, Tohoku University, Sendai 980-8577, Japan
[d] China Academy of Aerospace Standardization and Product Assurance, Beijing 100071, China

ARTICLE INFO

Keywords:
Laser cladding
B_4C/TiC ceramics particles
Microstructure
Microhardness

ABSTRACT

In order to study the effect of TiC/B_4C ceramic particles on the microstructure evolution and microhardness of Ni204-based cladding coating, TiC/B_4C/Ni204-based composite coatings were fabricated by laser cladding. The results showed that the TiC ceramic particles in the 30%TiC + 70%Ni204 coating do not decompose. TiC is the main reinforcing phase in the coating; however, in 30%B_4C + 5%TiC + 65%Ni204 composite coating, TiB_2 phase was *in situ* synthesized, and graphite, Fe_2B, Ti-Mo-Nb, (Ti, Nb, Mo)(B, C) were formed simultaneously in the coating. The addition of TiC promoted the dissolution and reaction of B_4C. In the presence of 30%TiC, the average microhardness and friction coefficient of the coating were 966.4 $HV_{0.5}$ and 0.198, respectively, which were 3.23 and 0.281 times of the initial Ni204 coating. In the presence of 30%B_4C and 5%TiC, the average microhardness and friction coefficient of the coatings were 1308.2$HV_{0.5}$ and 0.530, respectively, which were 4.38 and 0.752 times of the initial coatings. The enrichment of TiC is proportional to the hardness of the coating.

1. Introduction

Boron carbide (B_4C) has high hardness and melting point, good chemical stability, but has poor strength and fracture toughness, poor sintering performance and poor machinability [1,2]. B_4C is widely used in wear-resistant components owing to its hardness and wear resistance [3,4]. Ni-based alloy has excellent self-compatibility and good wettability with alloy matrix, but the hardness and wear resistance need to be further improved [5,6].

The Ni-based coating strengthened by ceramic particles has high hardness, excellent wear resistance, and corrosion resistance. Filippov et al. [7] fabricated the B_4C/Ni composite coating by cold spray first, followed by laser cladding technology to remelt the cold sprayed coating. After laser cladding, the porosity of the coating decreased and the boundary of the B_4C ceramic particles and matrix disappeared. Wang et al. [8] fabricated Ni-15%B_4C composite coatings by spark plasma sintering. The results showed that the diffusion rate of C atoms in Ni is faster than that of B atoms. The toughness of Ni-15%B_4C composite coatings is low, and the failure mode during the bending test is brittle fracture. Saroj et al. [9] studied the effects of different laser cladding parameters on the macro-morphology, particle distribution, and microstructure of titanium carbide (TiC)-Inconel825 composite coatings in tungsten inert gas atmosphere. Compared to AISI304 steel, the microhardness of TiC-Inconel825 composite coating increased by more than four times. The good wettability between Ni-based alloy and TiC improved the sliding abrasive wear resistance of the coating. Xu et al. [10] investigated the effect of TiC on the nucleation, microstructure evolution mechanism, and properties of Inconel624 coating fabricated by laser cladding. The uniformly distributed TiC ceramic particles refined the microstructure of the coating. The hardness increased from 220 HV to 330 HV, and the tensile strength reached 824 MPa.

The microhardness of TiC composite coatings is lower than that of B_4C composite coatings; however, B_4C composite ceramic materials exhibited inferior sintering properties [11] with low strength and toughness [3,4]. These fatal shortcomings limit the application of B_4C. Deng et al. [2] produced B_4C/TiC/Mo ceramic composite coating by hot pressing. The compact B_4C/TiC/Mo composite formed during hot pressing, and the degree of compactness increased with increasing TiC content. The hot pressing temperature of TiC/B_4C/Mo was lower than that of pure B_4C, and the fracture toughness, hardness, and bending strength of the composites increased by 10%. Yilbas [12] prepared TiC/B_4C composite coatings without pores and cracks on the zirconia surface by laser ablation. The self-annealing effect produced by multiple

* Corresponding author at: School of Mechanical Engineering and Automation, Northeastern University, Shenyang 110819, China.
E-mail address: tianbiaoyudyx@gmail.com (T. Yu).

https://doi.org/10.1016/j.ijrmhm.2019.105112
Received 26 June 2019; Received in revised form 29 August 2019; Accepted 22 September 2019
Available online 17 October 2019

scanning could reduce the stress, thereby the cracks disappeared. The unmatched thermal expansion coefficient between the ceramic particles and matrix generated some pin holes in the coating. Friction coefficient also decreased because of crack-free and high hardness. Popov et al. [13] studied the reaction mechanism of TiC-B_4C at high temperature. Boron on the surface of B_4C diffused into TiC through gas phase at ≥1700 °C, and TiB_2 was *in situ* synthesized accompanied by the formation of graphite. Rejil et al. [14] fabricated AA6360/(TiC + B_4C) hybrid surface composite layer (SCL) by friction stir processing and studied the effect of TiC and B_4C contents on the sliding friction properties and microstructures of SCL. 50% TiC and B_4C had the lowest wear rate and the lowest iron content in wear debris. The addition of TiC and B_4C increased the plastic flow resistance of AA6360 alloy. The reinforced phases in the SCL distributed evenly without segregation, and the reinforced particles had small size and less pointed shape at the reinforced particles boundary. Sun et al. [15] characterized the microstructure and mechanical properties of laminated B_4C/TiC composite fabricated by reactive melt infiltration on the Si and Al40Si60 alloy surface. The results showed that TiB_2 was formed by the reaction between TiC and B_4C. Multilayer structures with compressive stress layers could change the direction of cracks. Based on these literature reports, it is important to investigate the effect of adding TiC/B_4C on improving the fracture toughness, microhardness, wear resistance, and other mechanical properties of composites. TiC/B_4C composite has been extensively prepared by sintering and hot pressing, while a few reports mentioned the preparation of B_4C/TiC composite coatings by laser cladding technology.

In this study, Ni-based composites with 30%TiC and 5%TiC + 30% B_4C were produced by laser cladding. The microstructure and mechanical properties of the composites were studied, especially the effect of TiC addition on the properties and microstructure of B_4C/Ni-based composites.

2. Experimental

No. 45 steel with the size range of 100–100-10 mm was used as the substrate, and its chemical composition is listed in Table 1. Before using, the surface of the substrate should be sanded and then washed with alcohol, and dried. Ni204 was chosen as the initial powder in this experiment because of its good formability. The chemical composition of Ni204 powder is listed in Table 1 (provided by supplier). Ni204 powder comprises round particles with 100–270 meshes (53–150 μm). The microhardness of Ni204 cladding layer is between 300 $HV_{0.5}$ and 320 $HV_{0.5}$, and the friction coefficient between Ni204 and ZrO_2 ball is between 0.64 and 0.71 (reported previously by us). In order to enhance the properties of initial Ni-based powders, TiC (99% purity, 6–10 μm) and B_4C (99.9% purity, 2–3 μm) powders were selected to reinforce the Ni204 coating. The composite powder and process parameters of different compositions are listed in Table 2. Ceramic balls with the diameters of 8 and 6 mm were used as the mixing media, and their ratio with powders was 2:1. Before mixing, the powder was dried in a dryer at 120 °C for 4 h at constant temperature. Then, the powder was mixed at a rotating speed of 30 r/min for 2 h. After mixing, the powder was dried at 120 °C for 4 h in a dryer.

The required coatings were prepared using an open-loop control system consisting of a 6-DOF KUKA robot, powder feeder, YLP-500 IPG laser, coaxial powder feeding laser head, water cooler, and control system [16]. During the cladding process, Ar gas functioned as the shielding gas and powder feeding gas. Ar gas would not react with Ni204-based alloy, TiC, B4C, and had no effect on the experimental results. The experimental principle of laser cladding is shown in Fig. 1 [17]. All the coatings were prepared at room temperature.

After laser cladding, all the samples were cut along vertical and horizontal directions, and the surface was polished with sandpaper until the size of sandpaper reaches #2000 and polished with diamond polishing paste. The cross section of the sample was washed with alcohol and corroded 120-150S with $HCl:HNO_3:H_2O$ = 2:1:1. The microstructure, surface morphology, and composition of the samples were observed by laser confocal microscopy (LCM, LEXTOLS4100) and scanning electron microscopy (SEM, ULTRA PLUS). The phases in the samples were characterized by X-ray diffraction (XRD, X Pertpro) equipped with the Cu Kα radiation at 2.2 kW. The microhardness distribution along the depth section of the coating was measured using a Vickers microhardness tester EM500-2A. The load was 500 gf, the loading time was 10 s, and the distance between the two adjacent test points was 80 μm. The wear properties of samples with different compositions were measured using a MFT-4000 reciprocating friction and wear tester. ZrO_2 ceramic balls (HRC > 90) with a diameter of 5 mm were selected for a pair of grinding parts. For the wear process, the weight of 1 kg was chosen as the load. The reciprocating distance is 5 mm, the speed is 200 mm/min, and the reciprocating time is 30 min.

3. Results and discussion

3.1. Phase compositions and microstructure

Fig. 2 shows the XRD diffraction peaks of samples 2 and 3. When 30%TiC was added to Ni204, the main phases in the sample 2 coating are TiC, Ni-Cr-Fe, [Ni, Fe], and Ni-Cr-Nb-Mo. The melting point of TiC is 3140 °C, and it has high thermal stability during laser cladding [10], and the TiC particles did not react with the elements in Ni204 alloy powder. In 5%TiC/30%B_4C/65%Ni204-based composite coatings (sample 3), TiC, B_4C, graphite, TiB_2, Fe_2B and Ni-Cr-Fe were detected. Graphite, TiB_2 and Fe_2B are the new phases, and TiB_2 and graphite formed from the reaction of TiC and B_4C; however, TiC was still detected in sample 3, indicating incomplete reaction. The reaction Eq. is as follows [18]:

$$B_4C + 2TiC \rightarrow 2TiB_2 + 3C \quad (1)$$

According to the thermochemical data of B_4C-TiC system [19], the Gibbs free energy of formula (1) was −201.800 kJ/mol at 2100 K [20]; therefore, based on Eq. (1) TiB_2 and graphite could form during laser cladding.

Slight decomposition of B_4C occurs during the cladding process, and Fe and B_4C reacted more easily than Ti and B_4C during the cooling process [21]. In addition, the absolute value of free energy of Fe_2B reaction is greater than that of other borides; therefore, Fe_2B is thermodynamically most stable and easy to form [22]. Fe_2B was observed in the Fe/Ti/B_4C composite coatings prepared by Wang et al. [23]. It was confirmed that Fe reacted with B_4C to form Fe_2B in sample 3 composite coatings.

Fig. 3 shows the EDS mapping analysis results of B, C, Ti, Mo, Nb, Cr, Si, Ni, and Fe in the enhanced phase region generated by sample 3. The position of 1, 1-1, 2, 2-1, and 4 in Fig. 3(a) was analyzed by EDS, and the energy spectrum analysis is listed in Table 3. At least six phases were observed in the microstructure. Combining the XRD test results of

Table 1
Chemical composition and proportion of #45 steel and Ni204 powder.

	C	P,S	Si	Cr	Ni	Mn	Mo	Nb	Cu	Fe
Ni204	≤0.03	–	0.4	21	Bal.	–	9	4	–	1.5
45 steel	0.42–0.5	≤0.045	0.17–0.37	≤0.25	≤0.25	0.5–0.8	–	–	≤0.25	Bal.

Table 2
Composition ratio of different composites and laser cladding parameters.

Sample no.	Component content (wt%)				Laser cladding parameters				
	Ni204	TiN	TiC	B_4C	Laser power (W)	Scan speed (mm/s)	Powder feeding rate (rpm)	Overlap distance (mm)	Adjacent layers distance (mm)
1	100	0	0	0	450	5.5	0.7	0.85	0.35
2	70	0	30	0					
3	65	0	5	30					

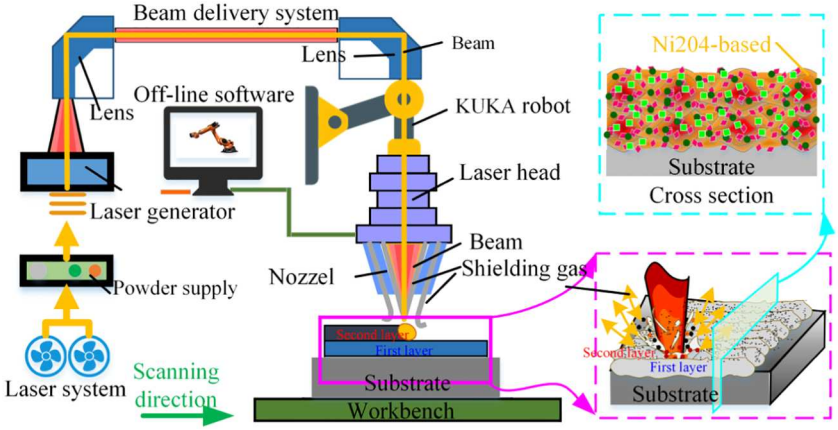

Fig. 1. Experimental principle.

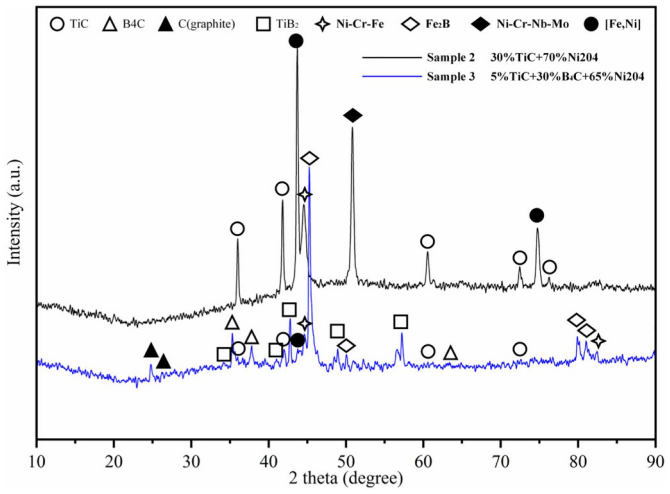

Fig. 2. X-ray diffraction of samples 2 and 3.

Fig. 2 indicates the first phase as graphite (i.e., Fig. 3(a)1 and 1-1). Fig. 3(a)1 and 1-1 regions have 87% and 85% C atoms, respectively (Table 3). The phase was further determined mainly as the graphite; the second phase was TiB_2 ceramic phase, which was rich in Mo and Nb (i.e., Fig. 3(a)2 and 2-1). Within Fig. 3(a)2 and 2-1 regions, B:Ti was larger than 2 (Table 3). A large number of C elements detected might be due to the fact that the residual B_4C did not react fully with TiC or the graphite formed after the reaction with TiC, and failed to fully diffuse out. While the C atoms did not enrich due to the presence of Mo elements [24,25], the dispersion distributed in TiB_2 (i.e., Fig. 3(c)); the third phase was rich in Ti, Mo, and Nb with a small amount of B and C, in which the B content was higher than that of C (i.e., Fig. 3(a)3); the fourth phase is rich in Ti, Mo, Nb, and B with a small amount of C (i.e., Fig. 3(a)4). According to the results of He et al. [26] and the energy spectrum analysis of Table 3, the phase was further determined as (Ti, Nb, Mo)B and (Ti, Nb)C; the fifth phase was Fe_2B, which was rich in Cr and Mo. Fe_2B mainly appeared near the TiB_2 ceramic particles (i.e., Fig. 3(a)5, and the phase mainly distributed around Fig. 3(a)1 and 2); the sixth phase was rich in Ti, Mo, and Nb (i.e., Fig. 3(a)6).

In laser cladding process, ceramic particles absorb energy more easily than Ni-based alloys [27]; therefore, ceramic particles could be dissolved. The melting point of B_4C is 2350 °C and lower than that of TiC. The B atoms on the surface of B_4C ceramic particles were easier to diffuse to TiC [13]. Therefore, the B atoms in B_4C combined with Ti atoms in TiC to in-situ synthesize TiB_2 [18]. At the same time, graphite appeared on the periphery of TiB_2 phase. Some unreacted B_4C was observed at the junction of graphite and TiB_2 and the periphery of graphite phase (i.e., 1, 1-1, 2 and 2-1 in Fig. 3(a)). This result was confirmed by the XRD analysis of sample 3 in Fig. 2 and EDS mapping analysis in Fig. 3(b)–(g). The presence of Mo affected the diffusion of Ti, Nb, C, and B in liquid, changed the solidification rate, promoted the precipitation of boride, and increased the size of boride [26]. Ti dissolved in NbB and Nb_2C, formed by the eutectic reaction of Nb-C-B, formed (Nb, Ti)C, and (Nb, Ti)B solid solution [28], and then formed (Nb, Mo, Ti)(B, C) with Mo [26,29–31]. The biggest difference between the third and fourth phases was different contents of B and C, as determined by Fig. 3(b)–(g). The binding ability of Fe and B around TiB_2 ceramic particles is higher than that of Ti [21]. Therefore, Fe_2B phase was detected in sample 3 and mainly appeared near the TiB_2 ceramic particles, as shown in Fig. 3(a)5. In the laser cladding process, Mo was not suitable for solute of TiC in the cladding layer, but it could accelerate nucleation and refine phase [25]. The existence of Mo retarded the coarsening behavior of carbides. The growth of carbides was basically in the form of (Ti, Nb)C [24,25]. Therefore, the phase similar to that in the region of Fig. 3(a)6 was mainly Ti-Nb-Mo solid solution with no enrichment of C and B. Ti and C elements can precipitate from the matrix to form fine TiC particles [32,33].

Fig. 4 shows the EDS line scan results of Ti, C, Nb, and Mo elements in Sample 2 and the enhanced phase spectra of different shapes. Combining with the XRD test results of Fig. 2, the black reinforcement phase particles were TiC ceramic phase. TiC was dissolved in the matrix formed by Ni204 alloy, agglomeration, and coarsening of TiC ceramics resulting in the formation of larger particles of TiC ceramics. The gray-white areas around the TiC phase were mainly Ti, C, Nb, and Mo

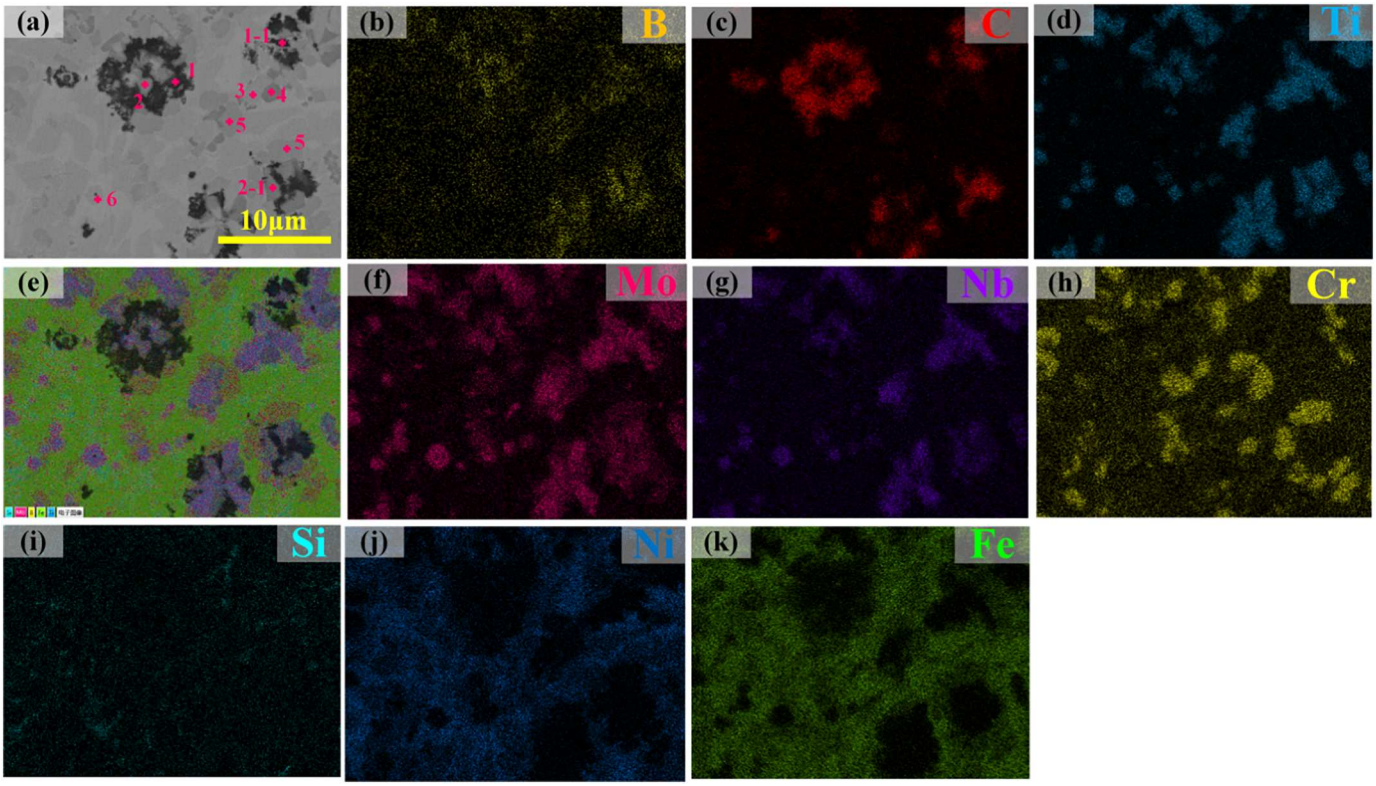

Fig. 3. EDS mapping analysis results of B, C, Ti, Mo, Nb, Cr, Si, Ni, Fe in sample 3.

Table 3
EDS analyses of sample 3# coating (in wt%).

Marked locations		C	Ti	B	Cr	Fe	Ni	Nb	Mo
1	wt%	59.72	9.07	–	11.05	9.62	2.70	2.69	4.51
	at. %	87.54	3.33	–	3.74	3.03	0.81	0.51	0.83
1–1	wt%	55.91	13.88	–	5.38	7.44	5.96	4.76	5.72
	at. %	85.98	5.35	–	1.91	2.46	1.87	0.95	1.10
2	wt%	25.46	25.71	16.15	9.82	2.11	1.04	8.15	11.57
	at. %	46.06	11.66	32.45	4.10	0.82	0.38	1.90	2.62
2–1	wt%	22.74	29.09	19.56	7.12	1.36	0.64	8.88	10.61
	at. %	40.38	12.96	38.6	2.92	0.52	0.23	2.04	2.36
4	wt%	15.79	36.96	13.77	7.9	1.67	0.81	10.43	12.67
	at. %	34.60	20.31	33.52	4.00	0.79	0.36	2.95	3.48

elements. Further coarsening of TiC particles were hindered by the presence of Mo [24,25], the ring phase around TiC was (Ti, Nb, Mo)C [29–31]. Compared to sample 3, the reinforcing phases in sample 2 was simpler and were mainly TiC and ring phase (Ti, Nb, and Mo)C around the TiC particles. The addition of TiC initiated the reaction with B_4C, allowing the *in situ* synthesis of TiB_2 ceramic phase. The phase in sample 3 was more complex.

Fig. 5 shows the macro-morphology of the sample measured by confocal laser microscopy and scanning electron microscopy. Fig. 5(a)–(c) are the macro-morphology of the sample measured by LCM. Fig. 5(d)–(f) show the microstructure of the samples measured by SEM under high resolution. There were no obvious pores and cracks in the Ni204 coating, and the metallurgical bonding at the overlap area of

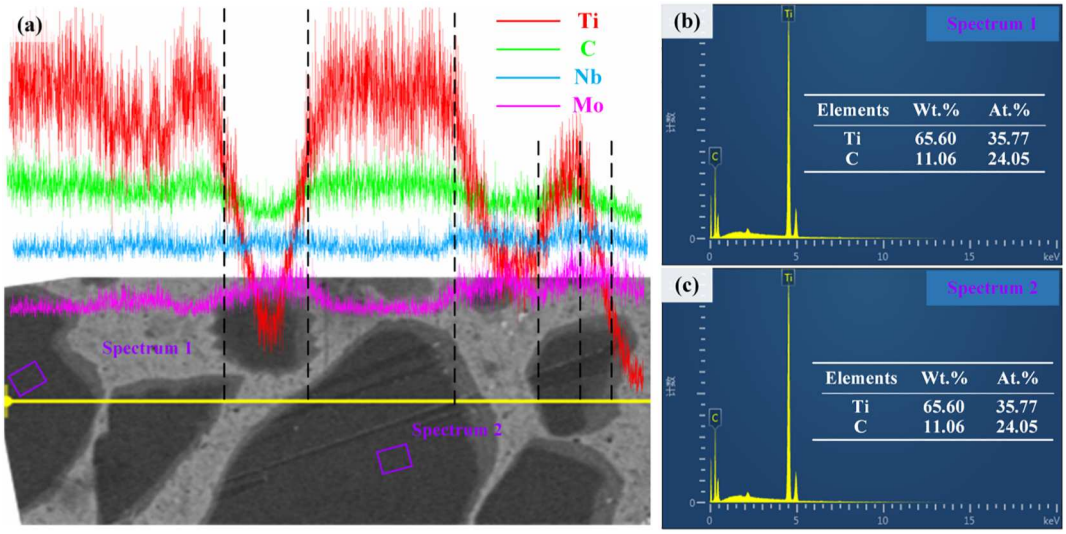

Fig. 4. EDS line scan and spectra of sample 3. (a), (b) EDS line scan of Ti, C, Nb, and Mo; (c) Spectrum 1; (d) Spectrum 2; (e) Spectrum 3.

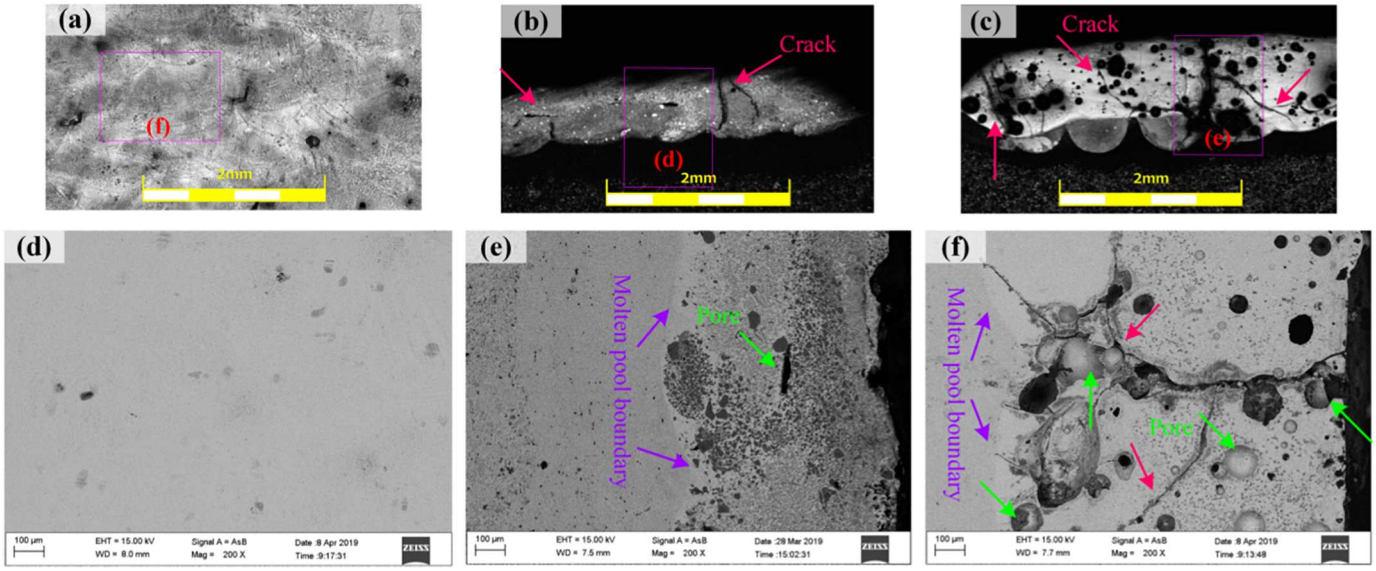

Fig. 5. Macro morphology of samples. Morphology of (a) Sample 1, (b) Sample 2, (c) Sample 3 by LCM; Morphology of (d) Sample 1, (e) Sample 2, (f) Sample 3 by SEM.

the clad tracks was good, as shown in Fig. 5(a). Within the 30%TiC + 70%Ni204 composite coating, the cracks mainly occurred in the overlap zone. Cracks were mainly caused by the agglomeration of TiC ceramics during laser cladding [33]. The metallurgical bonding in the overlap zone was good, and there were no pores, cracks, and delamination phenomena in the metallurgical bonding zone with the substrate. The metallurgical bonding quality was excellent, as shown in Fig. 5(b). The composite coating of 5%TiC + 30%B_4C + 65%Ni204 had a large number of pores and cracks, the direction of crack extension was tortuous, and the quality of metallurgical bonding with the substrate was good, as shown in Fig. 5(c). Fig. 5(d) shows the microstructure of sample 1 with 200× by SEM. There were no pores and cracks in the coating, and the metallurgical quality in the interlayer was good. According to Fig. 5(e), the distribution and size of TiC particles in sample 2 coating were relatively uniform. Fig. 5(f) shows the overlapped microstructure of sample 3 under scanning electron microscopy, indicating that the cracks meandering through the coating. TiB_2 was formed by the reaction of TiC with B_4C, and promoted the compactness of B_4C ceramics [34], reduced the porosity to some extent, but still was present. Previous studies show that the coatings containing B_4C particles has pores [1,35]. The one reason for the cracks might be due to the fact the thermal expansion coefficient of TiB_2 produced in the reaction process is higher than that of B_4C particles and probably increases the thermal stress of TiB_2 phase and surrounding coating, resulting in the formation of crack [35]. And the other reason might be the presence of the low-melting point phase. Sun et al. [18] reported that the cracks of pure B_4C coating extended along a straight line, but when TiC was added, the cracks were forced to deflect and expand, improving the winding degree of the coating. Therefore, the coating needed more energy when it broke. The specific ratios of TiC and B_4C to minimize the porosity and crack size need further study.

Fig. 6 shows the microstructure of the sample at different magnifications of SEM. Fig. 6(a)–(c) show the microstructure of sample 1 mainly containing dendrite, cell, equiaxed, and columnar crystals. The temperature gradient at the metallurgical bonding zone was large, and the grains were slender columnar and dendrite. The second phase precipitated on the grain boundary. According to the previous experiments, the second phase was [Nb, Mo]. Fig. 6(d)–(f) are the microstructure of sample 2. The addition of TiC refined the microstructure. With increasing temperature, the edges of TiC ceramic became smooth (i.e., Fig. 6(f)). With further increase in temperature, irregular TiC particles disappeared, but a large number of fine dendrites appeared [27], as shown in Fig. 6(d) and (e). The second phase [Nb, Mo] disappeared at the grain boundaries and mainly appeared around TiC particles in the form of (Ti, Nb, Mo)C ring phase. Fig. 6(g)–(i) are the backscattering method (BSM) images of sample 3. Under the BSM images, the areas of different colors in the coating were small and uniformly distributed in the coating. The elements of Nb and Mo mainly appeared in the form of Ti-Nb-Mo, (Ti, Nb, Mo)(B, C). TiC reacted with B_4C to form TiB_2 and eliminating C, thus formed the phenomenon of graphite surrounds TiB_2, which is consistent with the morphology observed by Popov et al. [36]. The addition of TiC led to the dissolution of B_4C in the coating and the formation of binary phase and multiphase with elements in the composite, for example, Fe_2B, TiB_2, graphite, TiC, B_4C, and Ti-Nb-Mo, (Ti, Nb, Mo) (B, C) phases.

3.2. Microhardness

Fig. 7 shows the microhardness distribution from the substrate to the coating surface. Fig. 7⑨ is the macrograph of the location of the microhardness test point of sample 3. The microhardness of the molten pool formed by sample 3 in the substrate is obviously divided from that formed on the substrate surface. The average microhardness of Ni204 coating was 298.9 $HV_{0.5}$ (measured by previous experiments). According to the results of microhardness test of sample 2 (as shown in Fig. 7), the microhardness of bulk of the enrichment TiC particles was 1339.7 $HV_{0.5}$. At this time, TiC particles had edges and corners, as shown in Fig. 7⑥. When the size of enriched TiC particles decreased, the apparent microhardness of the area was 968.6 $HV_{0.5}$. At this time, the edge smoothness of TiC increased, as shown in Fig. 7⑦. When the enrichment of TiC particles further decreased and became the dendritic crystal mode, the microhardness in this area was 457.2 $HV_{0.5}$, as shown in Fig. 7⑧. In the laser cladding process, the temperature inside the molten pool was the highest and the surface temperature of the coating was the lowest; therefore, the enrichment degree of TiC increased from the substrate to the coating surface, and the pointed shape of TiC particles became more obvious [27]. When the second layer was cladded, the TiC on the first layer surface could be remelted, improving the smoothness of TiC in the coating i.e., the microhardness of sample 2 coating increased gradually from the substrate to the coating surface. Regardless of the pores and cracks, the enrichment degree of TiC had a positive effect on microhardness. The average microhardness of sample

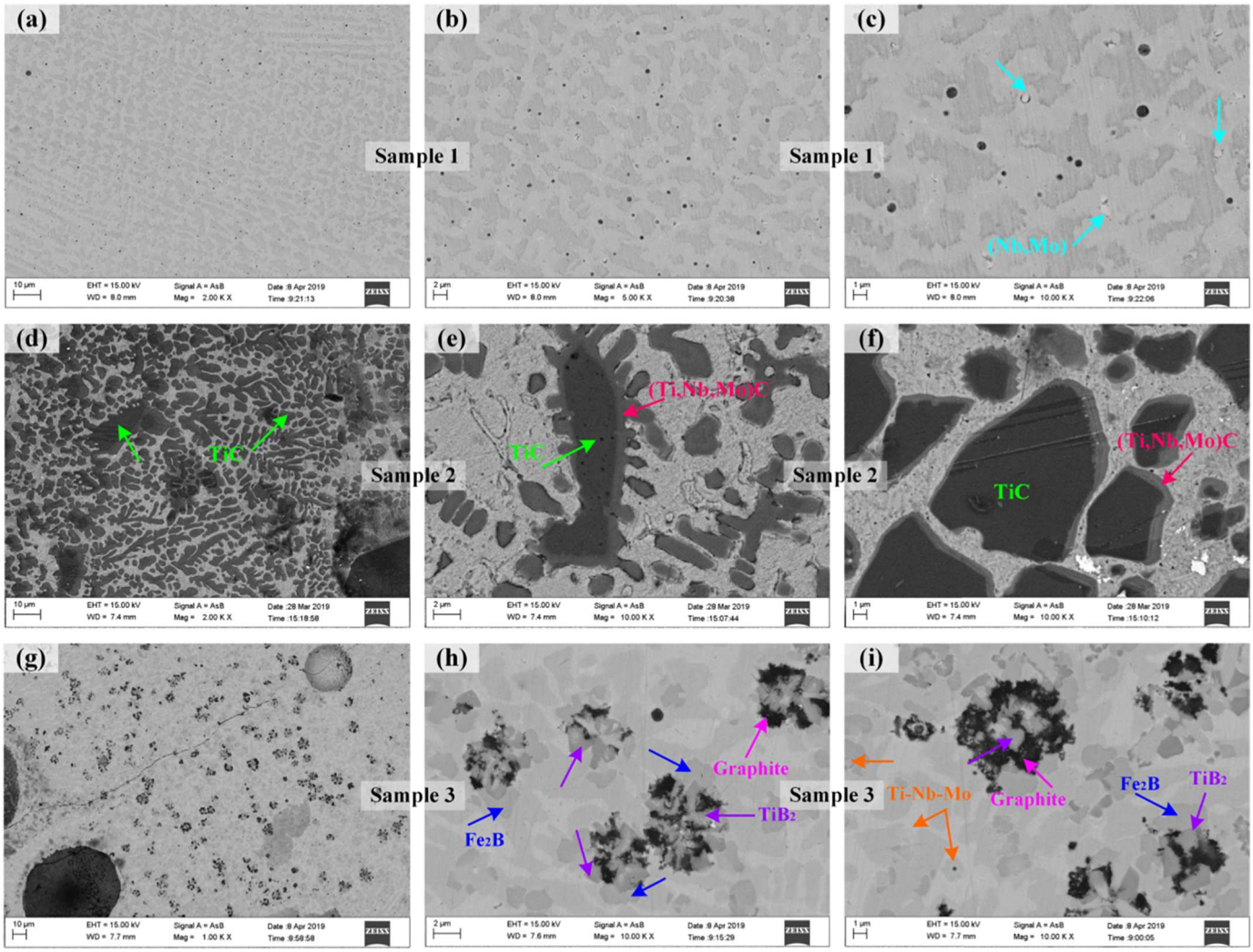

Fig. 6. SEM/BSE for samples. (a)–(c) Microstructure of sample 1(SEM); (d)–(f) Microstructure of sample 2(SEM); (g)–(i) Microstructure of sample 3(BSE).

2 was 966.4 $HV_{0.5}$, which was 3.23 times higher than that of the original Ni204 coating and 4.11 times higher than that of the substrate.

According to the test results of sample 3 (Fig. 7), the microhardness curve is divided into four regions: substrate (area 1), heat-affected zone (area 2), molten pool in the substrate (area 3), and molten pool on the substrate surface (area 4). The average microhardness of the area 3 is 687.4 $HV_{0.5}$, whereas that of the area 4 is 1308.2 $HV_{0.5}$. There is no transition zone between areas 3 and 4, and the boundary between them was clear and 4.38 times higher than that of the original Ni204 coating and 5.57 times higher than that of the substrate. The laser cladding decreased the heat dissipation rate of the coating and the number of dissolved B_4C particles in the coating increased, promoting the reaction between TiC and B_4C, *in situ* forming TiB_2 and Fe_2B. Although the hardness of TiB_2 is lower than that of B_4C, the formation of TiB_2 promoted the compactness of the structure of B_4C ceramics, thus increasing the microhardness of the coating [1,34]. The microhardness of TiB_2, graphite, and Fe_2B phase densely distributed area (i.e., Fig. 3(a)1 and 2) was the highest and found as 1457.3 $HV_{0.5}$, as shown in Fig. 7①. In the initial stage of the cladding, the temperature gradient was large, the heat dissipation of the cladding layer was fast, and the degree of reaction between B_4C and TiC was small and mainly dispersed in the coating. Due to the fact that most of the unmelted B_4C particles floated up during the cladding process, and the content of B_4C particles in the area 3 was low, the strengthening effect was weak, as shown in Fig. 7③. The microhardness was 679.1 $HV_{0.5}$. The microhardness at the all test points of area 4 was ≥1184 $HV_{0.5}$, as shown in Fig. 7④–⑤. The TiC promoted the diffusion of B atoms in B_4C. The TiB_2 and Fe_2B were *in situ* synthesized, together with the (Ti, Nb, Mo)(B, C), Ti-Mo-Nb, and other multiphase phases in the TiC/B4C/Ni204 composite coating. In addition, the unreacted B_4C dispersed in the coating, thus increasing the microhardness of the coating.

In Fig. 7⑨, the obvious layering occurred between the areas 3 and 4. However, with the progress of the experiment, this phenomenon disappeared. The microhardness distribution of the coating at L1 position in Fig. 8 was measured. The average microhardness of areas 3 and 4 is 1322.4 $HV_{0.5}$, similar to area 4 in Fig. 7. The main reason was that with the progress of the experiment, the temperature gradient of the coating decreased, and the amount of B_4C particles dissolved in the bottom of the coating increased, thus promoting the reaction of TiC, B_4C, and Ni204, changing the phase of the coating and increasing the microhardness.

3.3. Coefficient friction

Fig. 9 shows the time-dependent curve of the friction coefficients of the coating of samples 2 and 3. Before experiment, the samples should be sanded by sand paper and polished by polishing paste. The average friction coefficient of Ni204 coating was 0.705, which was abrasive wear when grinding with ZrO_2 ball. Compared to samples 2 and 3, the scratches were deep and scratches. In the initial stage of wear, the

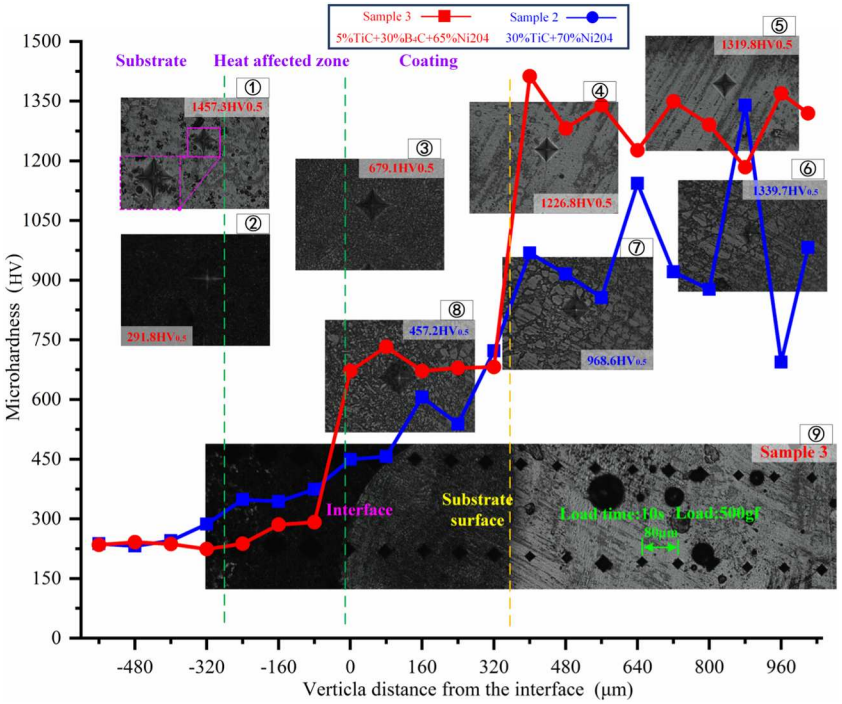

Fig. 7. The microhardness distribution along the cross section depth.

friction coefficient was unstable, and after the adaptive stage and the transitional wear stage (about 12 min later), it tended to be stable. The average friction coefficient of the specimen was calculated in 12–30 min and was 0.198 and 0.530 for samples 2 and 3, respectively. Compared to the initial powder Ni204 coating, the friction coefficient of the coating of samples 2 and 3 increased by 0.281 and 0.752 times, respectively.

Fig. 10 shows the wear morphology of samples. The wear width of Ni204 coating decreased by the addition of ceramic particles [37]. Fig. 10(a) and (b) are the macroscopic morphology of samples 2 and 3, respectively. The wear resistance of Ni204 coating improved by the reinforcement phase (TiC, B4C, TiB2, Ti-Mo-Nb, Fe2B, (Ti, Nb, Mo)(C, B)), which changed the grinding mechanism of Ni204 coating. According to Fig. 10(c), sample 1 mainly exhibits abrasive wear with deep plough groove scratches. Fig. 10(d) clearly shows that the uniform distribution of TiC ceramic phase in sample 2 coating effectively improves the wear resistance of the coating, with TiC phase as the main reinforced phase. TiC particles had the advantages of high hardness and wear resistance. When ZrO2 ceramic balls meet TiC in the wear process, TiC phase was difficult to destroy, thus effectively increasing the wear resistance of the coating. According to Fig. 10(e), graphite, TiB2, and Ti-Mo-Nb phases are clearly observed on the worn surface. TiB2 *in situ*

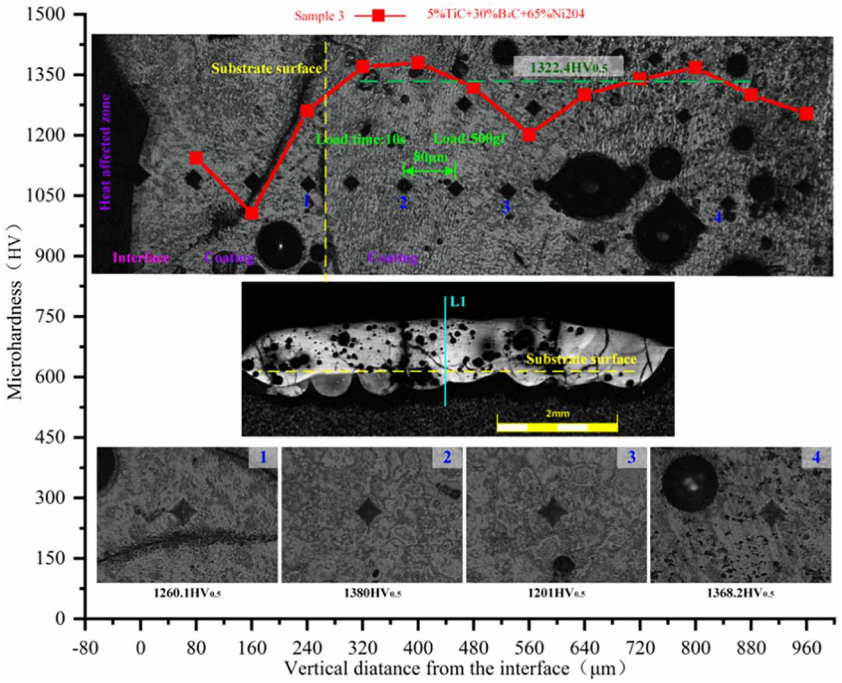

Fig. 8. The microhardness of sample 3.

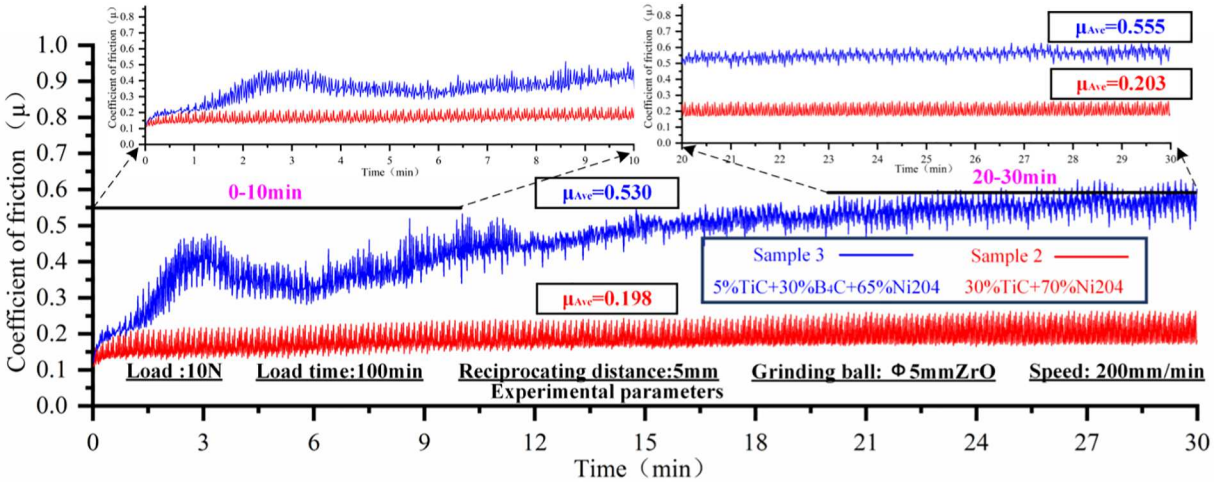

Fig. 9. Friction coefficient curves.

synthesized from TiC and B4C reduced the microhardness and improved the compactness of B4C; however, it was beneficial to improve the microhardness and wear resistance of the coating [1,14]. Graphite produced by the reaction also played a certain lubricating role in the wear process, improving the wear resistance of the coating and reducing the friction coefficient. However, the addition of B4C increases the number of cracks and pores in the coating and is not conducive to the improvement of wear resistance [1,18,35].

4. Conclusions

The 30%TiC/70%Ni204 and 5%TiC/30%B_4C/65%Ni204-based composite coatings were fabricated by laser cladding, and the characteristics of ceramic particles (TiC, B_4C) reinforced Ni204-based coating was studied. The conclusions of this study are as follows:

(1) In TiC/Ni204 composite coatings, TiC is the main reinforcement phase. The addition of TiC refines the microstructure. The Nb and Mo elements in the coatings also change from [Nb, Mo] in sample 1 to the Ni-Cr-Mo-Nb, (Ti, Nb, Mo) C ring phase around TiC particles. However, in TiC/B_4C/Ni204 coating, TiB_2 ceramic reinforcement phase was *in situ* synthesized by TiC and B_4C. The Nb and Mo elements in the coating exist in the form of (Ti, Nb, Mo)(B, C), Ti-Mo-Nb, etc. The Fe elements also combine with B elements in the coating to form Fe_2B phase.
(2) The microhardness of TiC/Ni204 coating increases with increasing

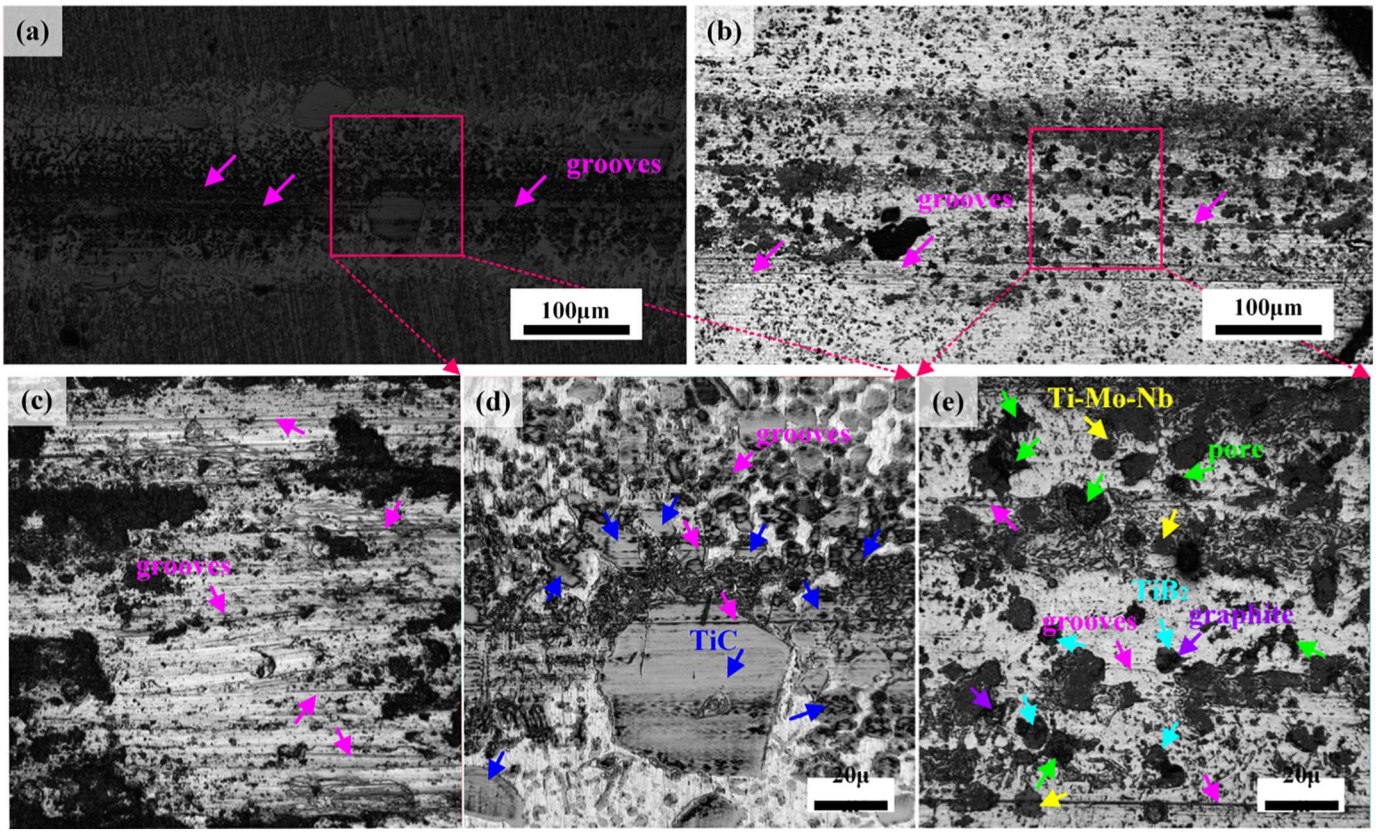

Fig. 10. Wear morphology. (a) Sample 2; (b) Sample 3; The enlarge images of (c) sample 1, (d) sample 2, and (e) sample 3.

degree of agglomeration TiC particles. The average microhardness of sample 2 coating is 966.4 $HV_{0.5}$, which is 3.23 times higher than that of sample 1. The average microhardness of the sample 3 coating is 1308.2 $HV_{0.5}$, which is 4.38 times higher than that of sample 1.

(3) The average friction coefficient of samples 2 and 3 is 0.198 and 0.530, respectively, and is 0.281 and 0.752 times higher than that of the Ni204 coating.

(4) The high content of B_4C particles in the Ni204 coating significantly improved the microhardness, but many tortuous cracks and pores were observed in the coating, affecting the wear resistance. The enriched TiC particles have distinct edges and corners, and the microhardness is 1339.7 $HV_{0.5}$ while the dispersed TiC particles have smooth edges. The microhardness of the areas of *in situ* synthesized TiB_2 and graphite with dense distribution is 1457.3 $HV_{0.5}$, and TiB_2, Fe_2B, Ti-Nb-Mo, and (Ti, Nb, Mo)(B, C) are the main phases in this area.

Declaration of Competing Interest

We declare that we have no financial and personal relationships with other people or organizations that can inappropriately influence our work, there is no professional or other personal interest of any nature or kind in any product, service and/or company that could be construed as influencing the position presented in, or the review of the manuscript entitled “Microstructure and properties of laser cladded B_4C/TiC/Ni-based composite coating”.

Acknowledgement

This study was support by the Fundamental Research Funds for the Central Universities (N180306004), the Ministry of Industry and Information Technology of China under Grant (No. 201675514), and the Science and Technology Planning Project of Shenyang under Grant (No. 18006001).

References

[1] M. Mashhadi, E. Taheri-nassaj, M. Mashhadi, V.M. Sglavo, Pressureless sintering of B_4C–TiB_2 composites with Al additions, Ceram. Int. 37 (2011) 3229–3235, https://doi.org/10.1016/j.ceramint.2011.05.096.

[2] D. Jianxin, S. Junlong, Microstructure and mechanical properties of hot-pressed B_4C/TiC/Mo ceramic composites, Ceram. Int. 35 (2009) 771–778, https://doi.org/10.1016/j.ceramint.2008.02.014.

[3] Y. Kanno, K. Kawsase, K. Nakano, Additive effect on sintering of boron carbide, J. Ceram. Assoc. Japan 95 (1107) (1987) 1137–1140, https://doi.org/10.2109/jcersj1950.95.1107_1137.

[4] J.X. Deng, Erosion wear of boron carbide ceramic nozzles by abrasive air-jets, Mater. Sci. Eng. A 408 (2005) 227–233, https://doi.org/10.1016/j.msea.2005.07.029.

[5] R. Vilar, A. Almeida, Repair and manufacturing of single crystal Ni-based superalloys components by laser Repair and manufacturing of single crystal Ni-based superalloys components by laser powder deposition — A review, J. Laser Appl. 27 (2016), https://doi.org/10.2351/1.4862697 S17004 1-7.

[6] M. Naghiyan, R. Shoja-razavi, H. Allah, H. Jamali, Microstructure investigation of Inconel 625 coating obtained by laser cladding and TIG cladding methods, Surf. Coat. Technol. 353 (2018) 25–31, https://doi.org/10.1016/j.surfcoat.2018.08.061.

[7] A.A. Filippov, V.M. Fomin, A.M. Orishich, Investigation of the microstructure of Ni and B_4C ceramic-metal mixtures obtained by cold spray coating and followed by laser cladding, AIP Conf. Proc. 1893 (2017), https://doi.org/10.1063/1.5007477 030019 1-5.

[8] M. Wang, W. Wang, H. Chen, Y. Li, Understanding micro-diffusion bonding from the fabrication of B_4C/Ni composites, International Journal of Minerals, Met. Mater. 25 (2018) 365–374, https://doi.org/10.1007/s12613-018-1580-0.

[9] S. Saroj, C.K. Sahoo, M. Masanta, Microstructure and mechanical performance of TiC-Inconel825 composite coating deposited on AISI 304 steel by TIG cladding process, J. Mater. Process. Technol. 249 (2017) 490–501, https://doi.org/10.1016/j.jmatprotec.2017.06.042.

[10] X. Xu, G. Mi, L. Xiong, P. Jiang, X. Shao, C. Wang, Morphologies, microstructures and properties of TiC particle reinforced Inconel 625 coatings obtained by laser cladding with wire, J. Alloys Compd. 740 (2018) 16–27, https://doi.org/10.1016/j.jallcom.2017.12.298.

[11] S.L. Dole, S. Prochazka, R.H. Doremus, Microstructural Coarsening During Sintering of Boron Carbide, J. Am. Ceram. Soc. 72 (6) (1989) 958–966, https://doi.org/10.1111/j.1151-2916.1989.tb06252.x.

[12] B.S. Yilbas, Laser texturing of zirconia surface with presence of TiC and B_4C: Surface hydrophobicity, metallurgical, and mechanical characteristics, Ceram. Int. 40 (2014) 16159–16167, https://doi.org/10.1016/j.ceramint.2014.07.047.

[13] H. Materials, O. Popov, A. Klepko, E. Lutsak, The in fluence of high pressure on TiC-B_4C reaction kinetics, Int. J. Ref. Metals 75 (2018) 234–237, https://doi.org/10.1016/j.ijrmhm.2018.05.004.

[14] C.M. Rejil, I. Dinaharan, S.J. Vijay, N. Murugan, Microstructure and sliding wear behavior of AA6360/(TiC + B_4C) hybrid surface composite layer synthesized by friction stir processing on aluminum substrate, Mater. Sci. Eng. A 552 (2012) 336–344, https://doi.org/10.1016/j.msea.2012.05.049.

[15] M. Sun, Y. Bai, M. Li, S. Fan, L. Cheng, Structural design of laminated B_4C/TiC composite fabricated by reactive melt in filtration, J. Alloys Compd. 765 (2018) 913–920, https://doi.org/10.1016/j.jallcom.2018.06.271.

[16] T. Yu, Y. Zhao, J. Sun, Y. Chen, W. Qu, Process parameters optimization and mechanical properties of forming parts by direct laser fabrication of YCF101 alloy, J. Mater. Process. Technol. 262 (2018) 75–84, https://doi.org/10.1016/j.jmatprotec.2018.06.023.

[17] T. Yu, J. Sun, W. Qu, Y. Zhao, L. Yang, Influences of z-axis increment and analyses of defects of AISI 316L stainless steel hollow thin-walled cylinder, Int. J. Adv. Manuf. Technol. 97 (2018) 2203–2220, https://doi.org/10.1007/s00170-018-2083-x.

[18] J. Sun, C. Liu, R. Wang, Low pressure hot pressing of B_4C matrix ceramic composites improved by Al_2O_3 and TiC additives, Mater. Sci. Eng. A 519 (2009) 27–31, https://doi.org/10.1016/j.msea.2009.06.016.

[19] P.D. Pan, X.G. Liu, X.Y. Sun, C.C. Wang, Fabrication and properties of ZrO_2/TiB_2 composite ceramic materials by in-situ synthesis, J. Synth. Crystals 41.3 (2012) 759–763, https://doi.org/10.16553/j.cnki.issn1000-985x (2012.03.017).

[20] J.L. Sun, Development of New B_4C Composite Ceramic Nozzle and Study on its Erosion Mechanisms, Shandong University Doctoral Dissertation, China, 2017.

[21] J.P. Wang, Fabrication of TiC + TiB_2 Locally Reinforced Carbon Steel Matrix Composites Using a (Ti, Fe)-B_4C System by SHS Reaction, Jilin University, 2008 Master Thesis.

[22] H. Fu, D. Fu, J. Xing, H. Fu, D. Fu, J. Xing, Investigations on the cast boron steel guide roller and its application in steel wire-rod mill, Mater. Manuf. Process. 23 (2) (2008) 123–129, https://doi.org/10.1080/10426910701774353.

[23] X. Wang, H. Shun, C. Li, X. Wang, D. Sun, The performances of TiB_2-contained iron-based coatings at high temperature, Surf. Coat. Technol. 201 (2006) 2500–2504, https://doi.org/10.1016/j.surfcoat.2006.04.025.

[24] J. Hoon, C. Lee, Y. Heo, D. Suh, Stability of (Ti, M)C (M = Nb, V, Mo and W) carbide in steels using first-principles calculations, Acta Mater. 60 (2012) 208–217, https://doi.org/10.1016/j.actamat.2011.09.051.

[25] J.H. Jang, Y. Heo, C. Lee, H.K.D.H. Bhadeshia, D. Suh, J.H. Jang, Y. Heo, C. Lee, H.K.D.H. Bhadeshia, D. Suh, Interphase precipitation in Ti–Nb and Ti–Nb–Mo bearing steel Interphase precipitation in Ti–Nb and Ti–Nb–Mo bearing steel, Mater. Sci. Technol. 29 (3) (2014) 309–313, https://doi.org/10.1179/1743284712Y.0000000131.

[26] X. He, X. Zhang, Y. Li, J. Huang, Effect of Mo on microstructure and mechanical properties of Nb–Ti–C–B multiphase alloy, J. Alloys Compd. 551 (2013) 578–583, https://doi.org/10.1016/j.jallcom.2012.11.052.

[27] R.L. Sun, J.F. Mao, D.Z. Yang, Microscopic morphology and distribution of TiC phase in laser clad NiCrBSiC–TiC layer on titanium alloy substrate, Surf. Coat. Technol. 155 (2002) 203–207, https://doi.org/10.1016/s0257-8972(02)00006-3.

[28] X. Zhang, X. He, C. Fan, Y. Li, G. Song, Microstructural and mechanical characterization of multiphase Nb-based composites from Nb–Ti–C–B system, Int. J. Refract. Met. Hard Mater. 41 (2013) 185–190, https://doi.org/10.1016/j.ijrmhm.2013.03.010.

[29] F. Wu, T. Chen, H.J. Wang, D.F. Liu, Effect of Mo on microstructures and wear properties of in situ synthesized Ti(C, N)/Ni-Based composite coatings by laser cladding, Materials 10 (2017), https://doi.org/10.3390/ma10091047 1047 1-12.

[30] G. Dong, J. Xiong, M. Yang, Z. Guo, W. Wan, Effect of Mo_2C on erosion–corrosion resistance behavior of Ti(C, N)-based cermets, Wear. 294–295 (2012) 364–369, https://doi.org/10.1016/j.wear.2012.05.013.

[31] E. Conforto, D. Mari, T. Cutard, The role of molybdenum in the hard-phase grains of (Ti, Mo)(C, N)–Co cermets, Philos. Mag. 84 (17) (2004) 1717–1733, https://doi.org/10.1080/14786430310001659516.

[32] X. Wang, X. Pan, B. Du, S. Li, Production of in situ TiB_2 + TiC/Fe composite coating from precursor containing $B_4C - TiO_2 - Al$ powders by laser cladding, Trans. Nonferrous Metals Soc. China 23 (2013) 1689–1693, https://doi.org/10.1016/S1003-6326(13)62649-7.

[33] Y. Cai, Z. Luo, M. Feng, Z. Liu, Z. Huang, Y. Zeng, The effect of TiC/Al_2O_3 composite ceramic reinforcement on tribological behavior of laser cladding Ni60 alloys coatings, Surf. Coat. Technol. 291 (2016) 222–229, https://doi.org/10.1016/j.surfcoat.2016.02.033.

[34] C. Xu, Y. Cai, K. Flodström, Z. Li, S. Esmaeilzadeh, G. Zhang, Spark plasma sintering of B_4C ceramics: The effects of milling medium and TiB_2 addition, Int. J. Refract. Met. Hard Mater. 30 (2012) 139–144, https://doi.org/10.1016/j.ijrmhm.2011.07.016.

[35] A. Moradkhani, H. Baharvandi, M. Mahdi, M. Samani, Mechanical properties and microstructure of B_4C–NanoTiB_2–Fe/Ni composites under different sintering temperatures, Mater. Sci. Eng. A 665 (2016) 141–153, https://doi.org/10.1016/j.msea.2016.04.034.

[36] O. Popov, S. Chornobuk, V. Vishnyakov, Structure formation of TiB_2-TiC-B_4C-C heteromodulus ceramics via reaction hot pressing, Int. J. Refract. Met. Hard Mater. 64 (2017) 106–112, https://doi.org/10.1016/j.ijrmhm.2017.01.012.

[37] F. Shu-rong, T. Hai-bo, Z. Shu-quan, W. Hua-ming, Microstructure and wear resistance of laser clad TiB-TiC/TiNi-Ti_2 Ni intermetallic coating on titanium alloy, Trans. Nonferrous Metals Soc. China 22 (2012) 1667–1673, https://doi.org/10.1016/S1003-6326(11)61371-X.